

# AIRCRAFT WING UNSTEADY THERMODYNAMIC CFD FOR PREVENTIVE-ICING SIMULATION

<sup>1</sup>Mr.Lijo Sebastian

<sup>1</sup> Asst. Manager in Designs – FAYAT Group, AMIE mech.

**Abstract:** A three dimensional (3-D) wing leading edge bay model and its two-dimensional (2-D) bay-slice approximation models are simulated using computational fluid dynamics (CFD). This computational fluid dynamics based model involves a complete wing segment including thermal anti-icing bay inside the leading edge. The unsteady, integrated internal/external thermal flow simulation is presented with heat conductivity through the solid skin in a structured mesh. The calculated skin temperature results are satisfactory in their good match with flight test data. The presented research work indicates a strong potential of using computational fluid dynamics in dynamic wing anti-icing system model development and validation. In this paper, a Navier-Stokes analysis is presented for a thermal aircraft wing anti-icing system. The numerical results and their comparative study address the 2-D approximation for the benefit of computational efficiency. Furthermore, the bay skin temperature distributions are obtained by an integrated interior–exterior thermodynamic analysis. It takes into account the skin heat transfer and conductivity. The 2-D CFD results may overestimate the heat transfer, but the surface temperature near the wing leading edge is within the flight test data range.

**Index Terms** - CFD analysis using ANSYS CFX, bay skin temperature distribution, internal/external thermal flow simulation, heat conductivity through the solid skin in a structured mesh ...

**M** = Mach number

**P, p** = static pressure (Pa)

**Po** = total pressure (Pa)

**t** = time (sec)

**T** = static temperature (K)

**To** = total temperature (K)

**U** = velocity (m/sec)

**$\alpha$**  = angle of attack (degree)

## I. INTRODUCTION

The research background comes from the necessity of developing a dynamic control technique for aircraft wing anti-icing system (WAIS). Fig. 1 shows a typical flowchart of such a system. The hot air from the turbo engine is introduced to the leading edge through pipes and valves. The control module regulates the wing anti-icing valve (WAIV) to control the heat flux into the Piccolo tubes in the leading edge anti-icing bays. It in turn adjusts the skin temperature of the wing leading edge. The control system works in a closed loop with the temperature sensors located at several points of the wing leading edge surface.

An efficient wing anti-icing control system development requires a dynamic thermal fluid model. It is a challenging task due to its complicated physics behavior in both anti- and de-icing flight operations. One well-received approach is to develop an empirical dynamic model of parameters that are tuned by flight test data, which are expensive and difficult to obtain, and even impossible in the early design phase. Instead, our research explores using the computational fluid dynamics (CFD) simulation data to assist in dynamic model development. Obviously unsteady simulations are required to serve this purpose.

CFD has been used in anti-icing research for years. Topics of recent work are mainly covered in the following two categories: 1) the CFD methods and software development to simulate the ice accretion process in external airflows with cold droplets. 2) Application of available CFD tools for aircraft anti-icing device design. Also presented their earlier work in steady Navier-Stokes simulations of the integrated internal/external thermodynamic simulations of two dimensional (2D) wing sections and three dimensional (3D) wing segments with WAIS. Structured meshes were generated for both hot internal bleeding air and cold external fields with heat conductivity through the wing skin. Simulation results visually revealed the hot/cold flow interactions and heat conductivity through the fluid and solid zones. Such steady CFD simulations provided useful observations for WAIS research and development.

In this paper, the 2D unsteady CFD simulations are first studied for time-dependent computations of WAIS under different hot air inlet conditions. They simulate the thermal flow under the adjustment of the control valves, and calculate the corresponding skin temperature. Then the 3D unsteady CFD model of WAIS is analyzed to simulate a complete anti-icing flight test loop. The calculated skin temperature results are found to coincide with the flight measurement very well. Therefore, the unsteady simulation results may be used in dynamic model tuning to complement or even re-create a flight test process.

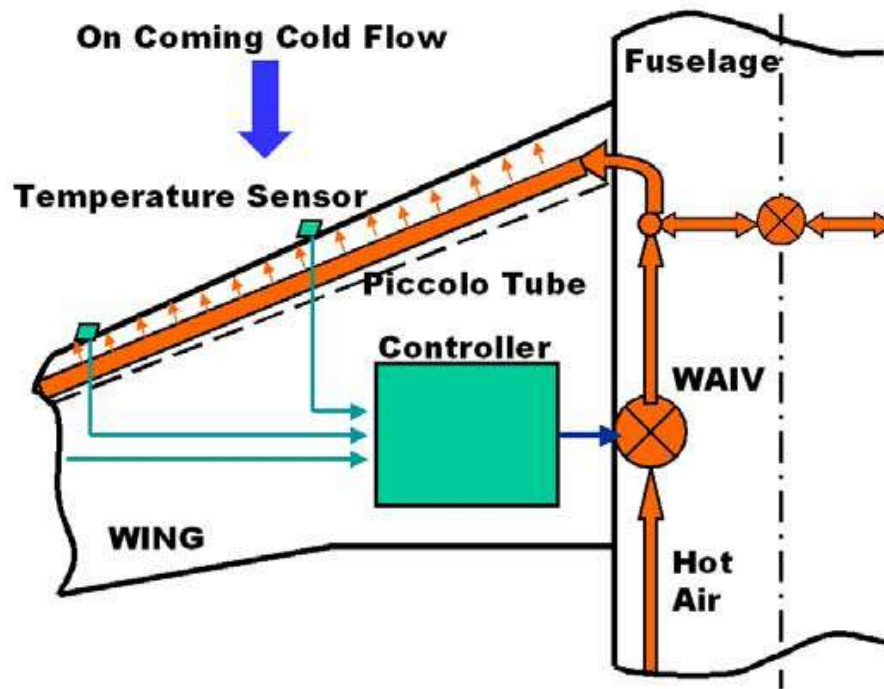


Fig. 1 Flowchart of a WAIS (left hand side only)

## II. FLOW FIELD ANALYSIS FOR A BAY MODEL

### 2.1. THE THREE-DIMENSIONAL BAY MODEL

The 3D wing span segment (Fig. 2b & 2c) consists of the following components. 1) A Piccolo tube introduces the hot air into the leading edge anti-icing bay. There are a number of small hoses on the front side of the Piccolo tube from where the hot jets impinge the inner surface of the leading edge. The small holes are located staggered in two rows of angles  $15^\circ$  upper and lower from the wing chord plane. 2) The aluminium skin is heated by the hot air in the anti-icing operation. 3) Two exhaust holes on the lower side of the bay allow the hot air to exit to the external flow. 4) Two ribs separate the bays in the span direction with the hoses on the ribs neglected. 5) The heat shield serves as the back wall of the bay. Structured meshes are generated for both internal and external flow

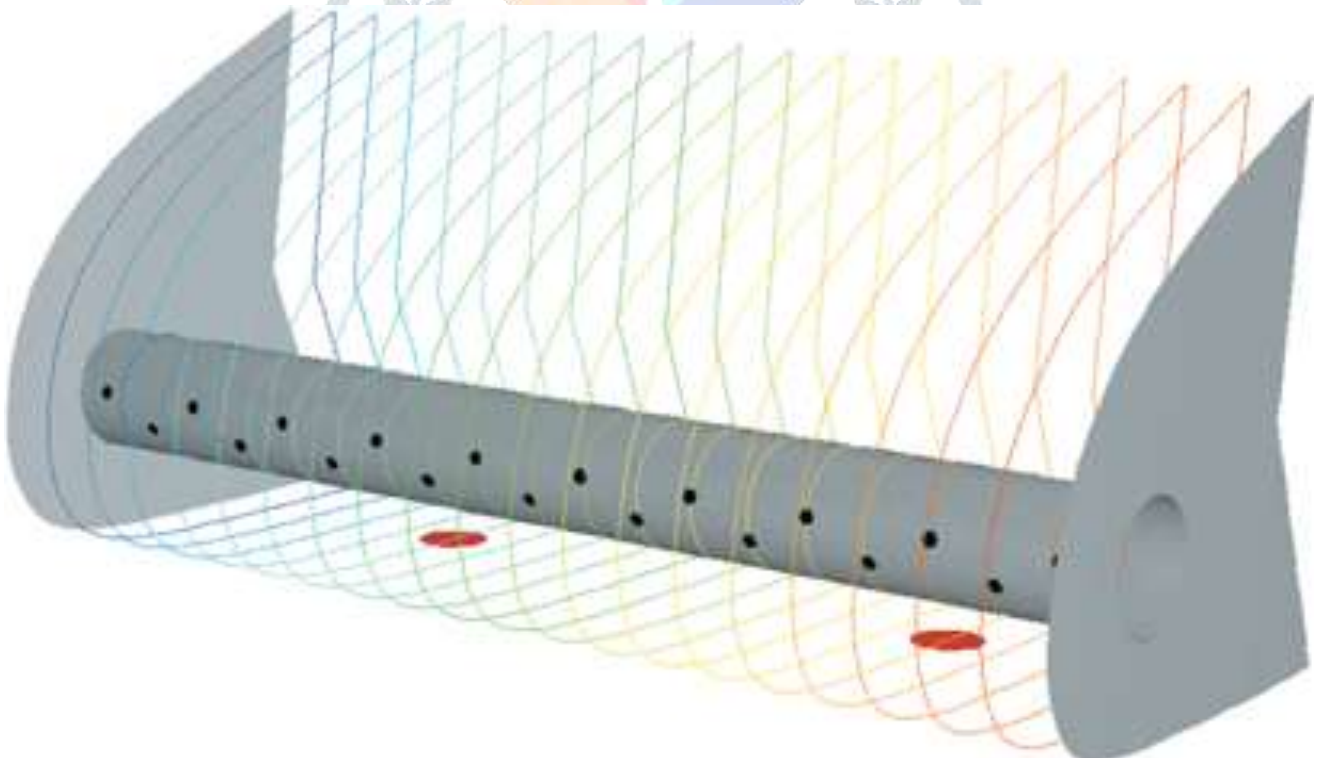
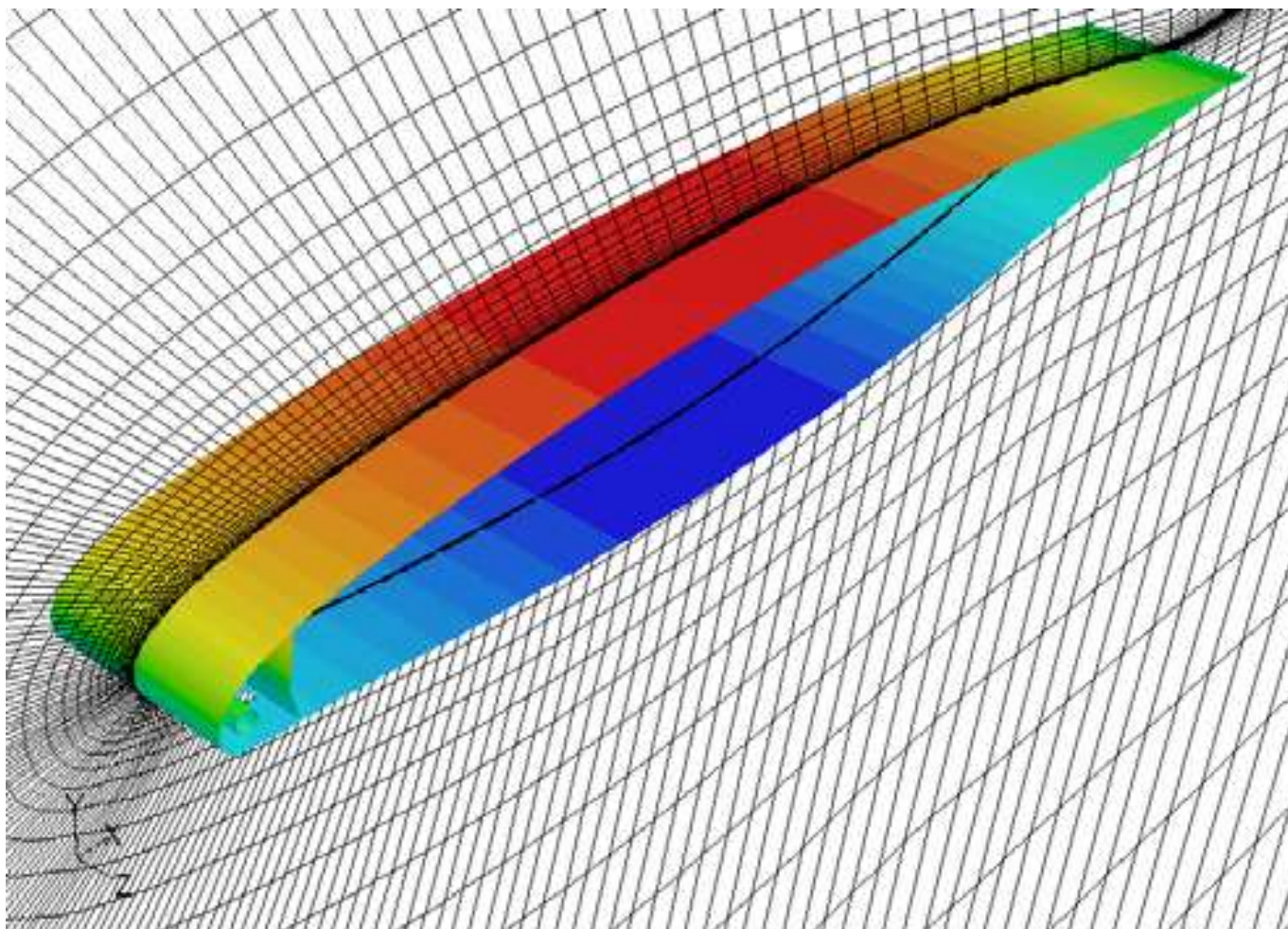


Figure 1. Three-dimensional bay model with two exhaust holes (the skin and heat shield shown by wires)





**Fig. 2b Wing segment with the thermal anti-icing bay (Shown with the mesh of a mid-span plane)**

Fields. The interior and exterior meshes are connected through the mesh in the exhaust holes. The diameter of the piccolo tube remains constant even though the bay itself is slightly tapered. A structured mesh is also used inside the aluminium skin for the heat conductivity calculation. The most important characteristics to us are the surface temperature distributions. The flow structure

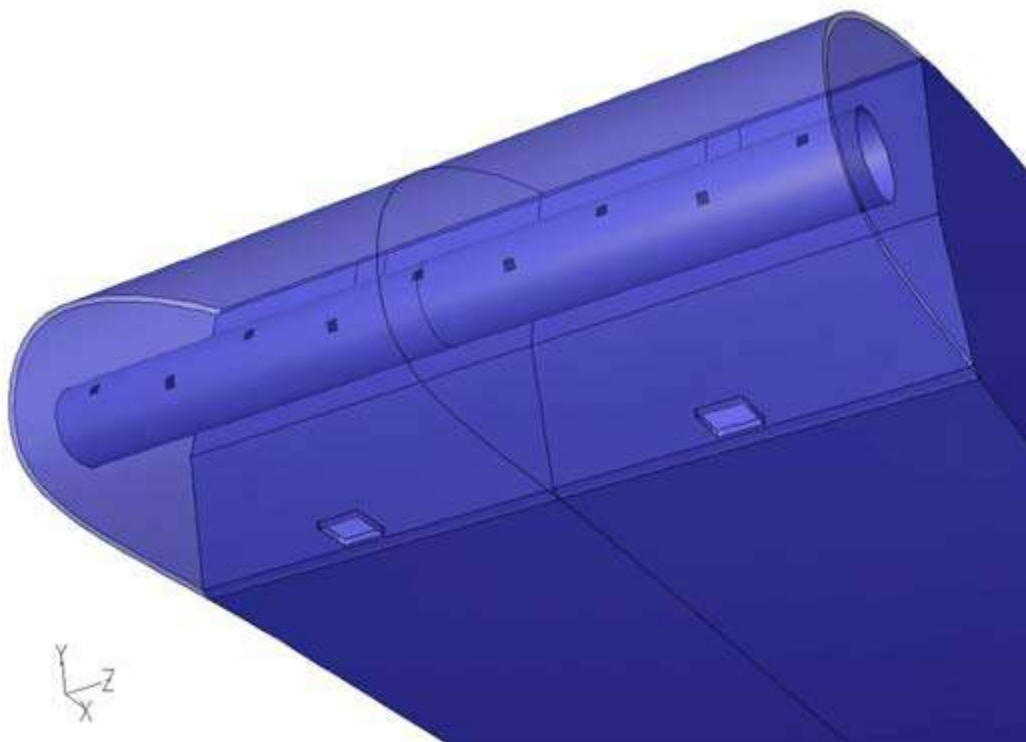


**Fig. 2c Leading edge anti-icing bay details**

Inside the bay is important for the heat transfer, and the global thermal efficiency  $\eta$ , defined below, is a major measure of the efficiency of the system:

$$\eta = (T_{inlet} - T_{exhaust}) / (T_{inlet} - T_{external})$$

where  $T_{inlet}$  represents the temperature inside the piccolo tube,  $T_{exhaust}$  is the temperature at bay exhaust holes, and  $T_{external}$  is the temperature at the flight altitude.

## 2.2. THE NUMERICAL APPROACH

The CFD analysis tool used in this research is a well-known commercial Navier-Stokes solver Fluent V6.0 (Fluent V6.0, 2002). Its reliability has been demonstrated by a large number of aerospace and industrial applications. An unstructured grid is used because of the complexity of the 3-D configuration. There are 281 980 nodes in the 3-D mesh and 21 330 nodes in the 2-D slice grid. Mesh adaption based on turbulent intensity is tested in 2-D simulations, but the results are found to be quite similar, as the original mesh is already fine enough. In the integrated interior–exterior thermal flow analysis, structured mesh is used. Details will be given later. One- and two-equation turbulent models are tested for the viscous flow simulation, and the RNG  $k-\epsilon$  Model, based on the renormalization group method, is selected because of its strength in simulating highly curved flows and wall heat transfers. Because the flow becomes compressible, the second order upwind schemes are used in both 2-D and 3-D.

Calculations. Pressure inlet and outlet conditions are used at the piccolo tube holes and the exhaust holes. The turbulent specification methods at the inlet boundary are the intensity and the hydraulic diameter, reflecting the size of the small holes. For the bay internal flow simulation, the inlet and outlet conditions are selected based on the flight test measurements (Bombardier Aerospace, 2002).<sup>1</sup> For example, one inlet condition is  $P = 90\,000$  Pa,  $T = 453$  K in the Piccolo tube, while the outlet condition is  $P = 63\,000$  Pa and  $T = 343$  K at the exhaust holes of the bay.

## 2.3. THE NUMERICAL RESULTS

**Figure 2** shows the velocity vectors colored by the velocity magnitude (m/s), injecting from the piccolo tube holes, flowing over the inner skin and the piccolo tube surfaces and draining through the exhaust holes. **Figure 3** plots part of the streamlines inside the bay. The flow in the lower part of the bay is mainly chord-wise and has higher speed. Mixed 3-D flow could be seen in the upper part of the bay, and clear cross flow exists near the upper-rear corner of the bay. However, because of the very small magnitude of the cross flow velocity, it may not significantly affect the values of the flow characteristics, such as the pressure and the temperature in the span direction there. Flow characteristics are examined to investigate the inference of the 3 D effects. **Figure 4** shows the skin friction coefficient  $C_f$  distributions. It is observed that the skin friction in the front leading edge is strong. The lower surface transfer is chord-wise dominant & the upper surface exchange is weak but roughly uniform.

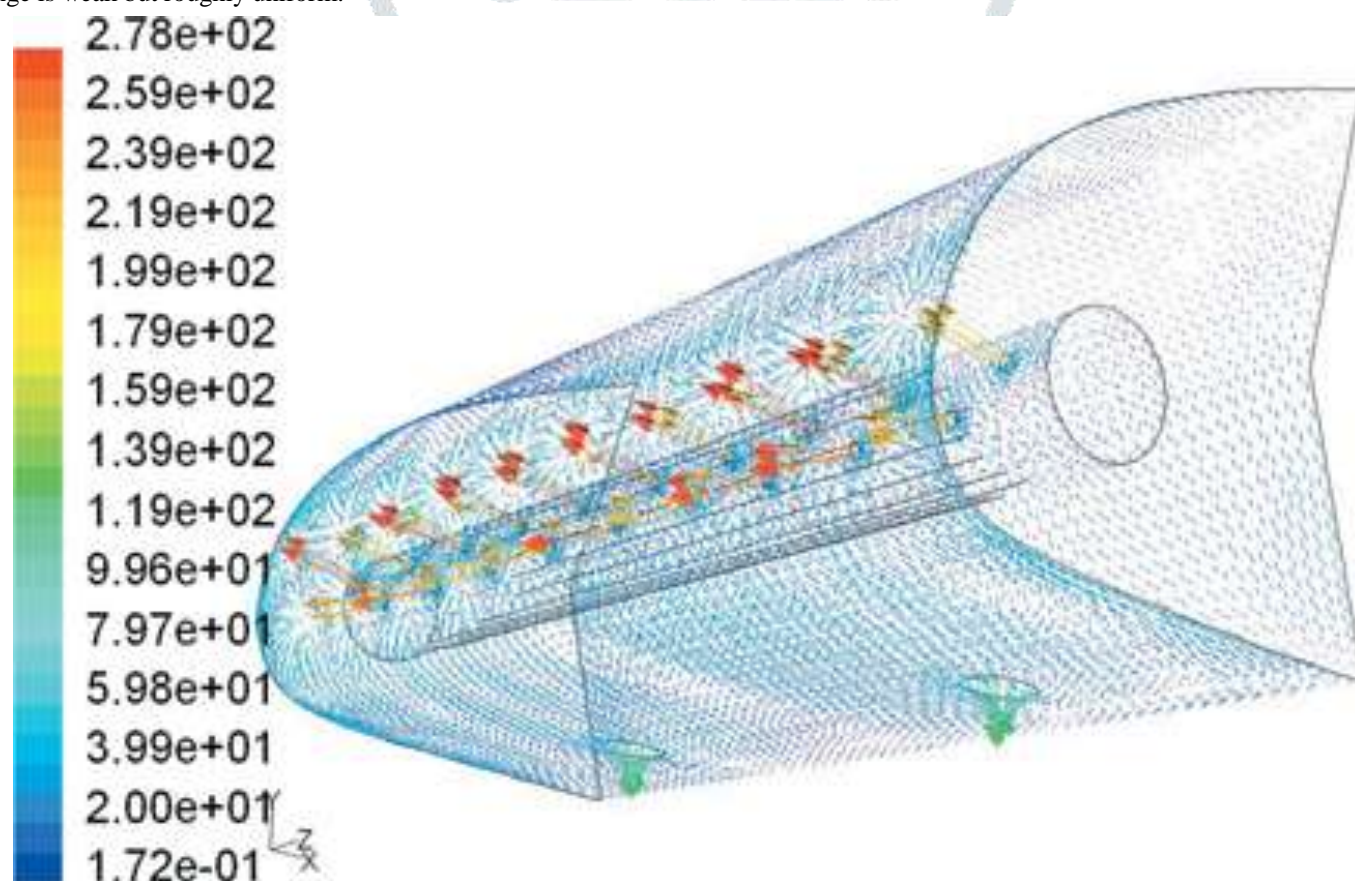


Figure 2. Velocity vectors (m/s).



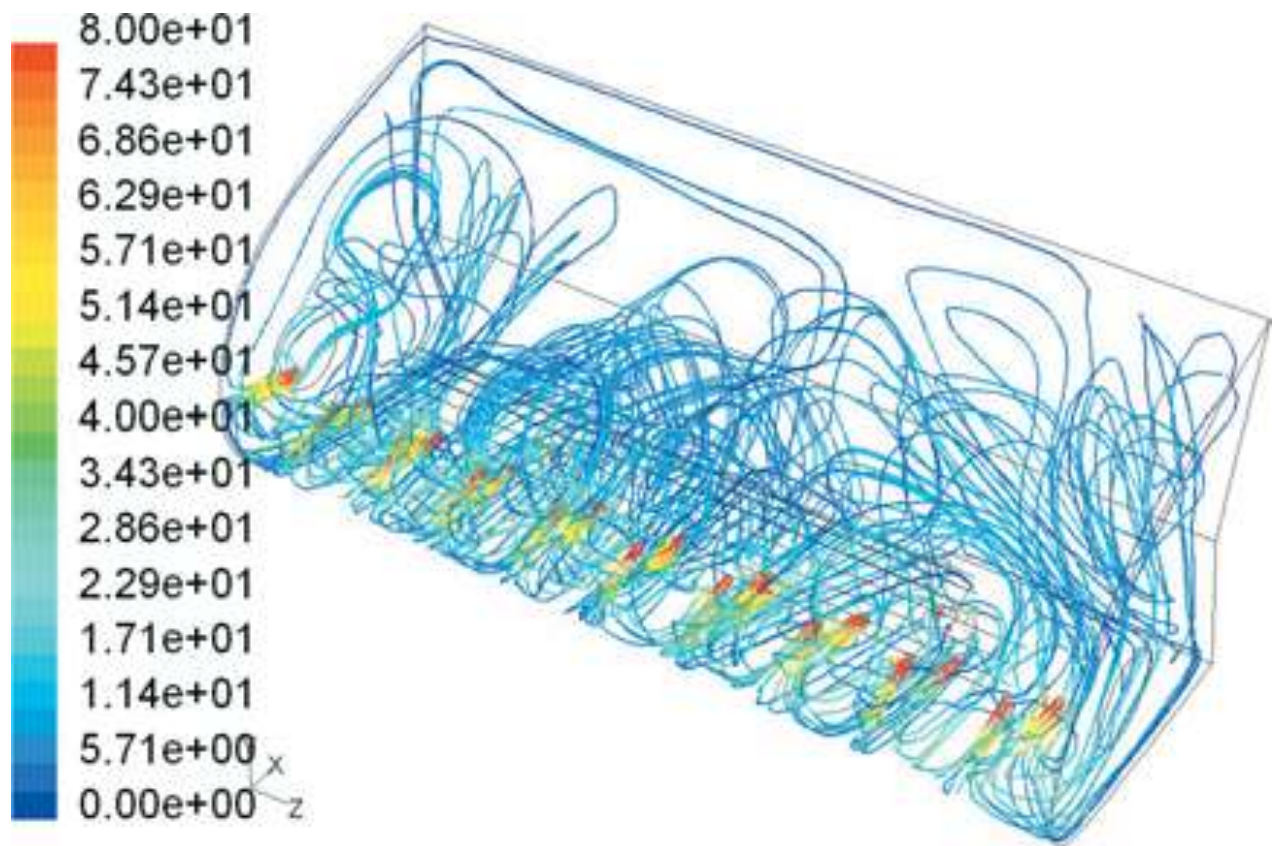


Figure 3. Part of the streamlines inside the bay (colored by velocity Magnitude (m/s)).

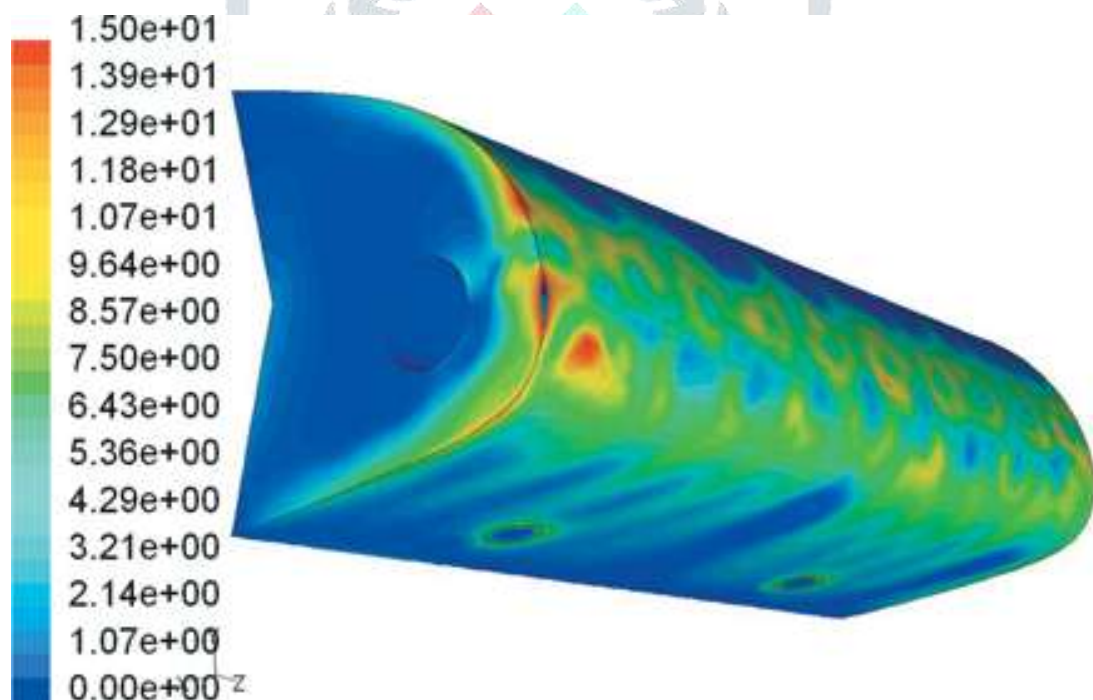
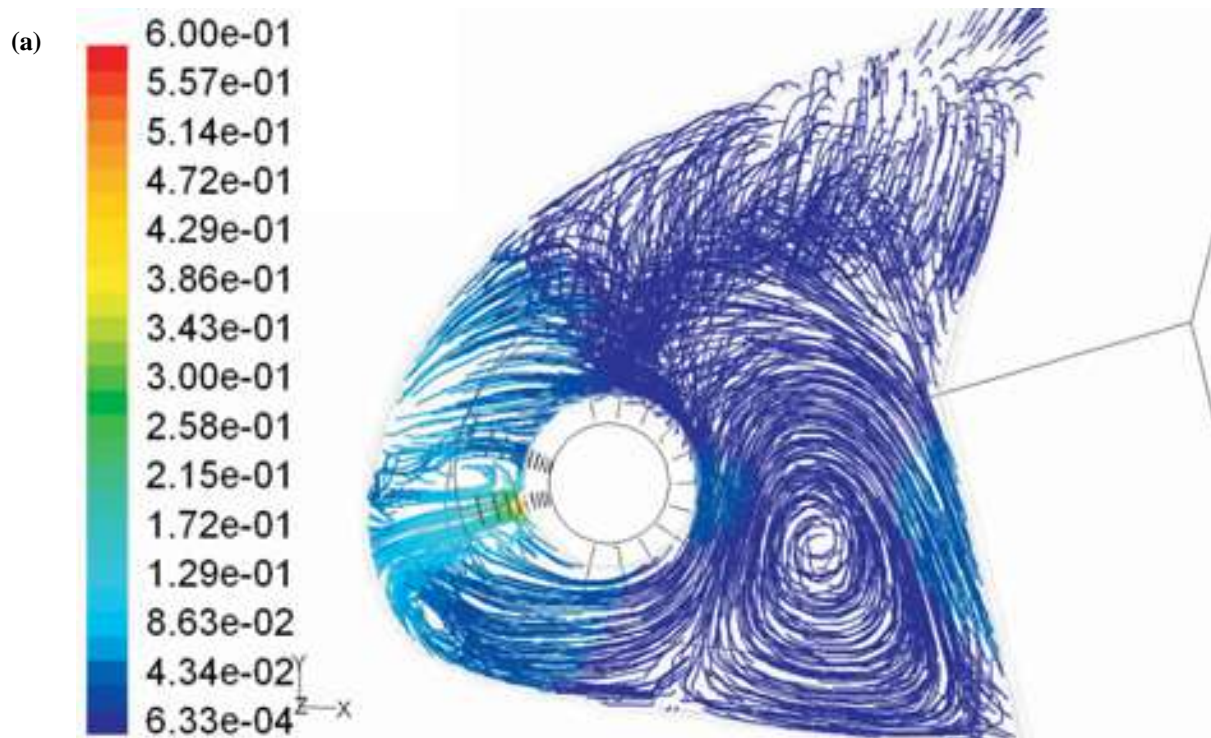


Figure 4. Skin friction coefficient distributions of the inner surface of the 3-D bay.

#### 2.4. COMPARISON OF THE TWO- AND THREE-DIMENSIONAL FLOW FIELDS

To evaluate the slice approximation assumption, 2-D slices are computed separately and compared with the flow fields of a couple of span sections of the 3-D bay, for example, the cross sections with and without injection holes, and those with and



Without exhaust holes. In the 2-D slice model, the injection and exhaust holes are modified into slots, the width of which is chosen to match the total injection and exhaust areas of the 3-D bay. Flow parameters, such as velocity  $V$ (m/s), Mach number  $M$ , the respective total and static pressures  $P_0$  and  $P$  (Pa), the total and static temperatures  $T_0$  and  $T$  (K), the skin friction coefficient  $C_f$  from both 2-D and 3-D computations, are also examined and compared, to further investigate the slice approximation. The streamlines of a 3-D section are compared with those of a 2-D slice in **Figure 5**. Both sections have a lower  $15^\circ$  injection, with the exception that an exhaust slot exists in the 2-D model. The injecting flow between the piccolo tube and the leading edge could be

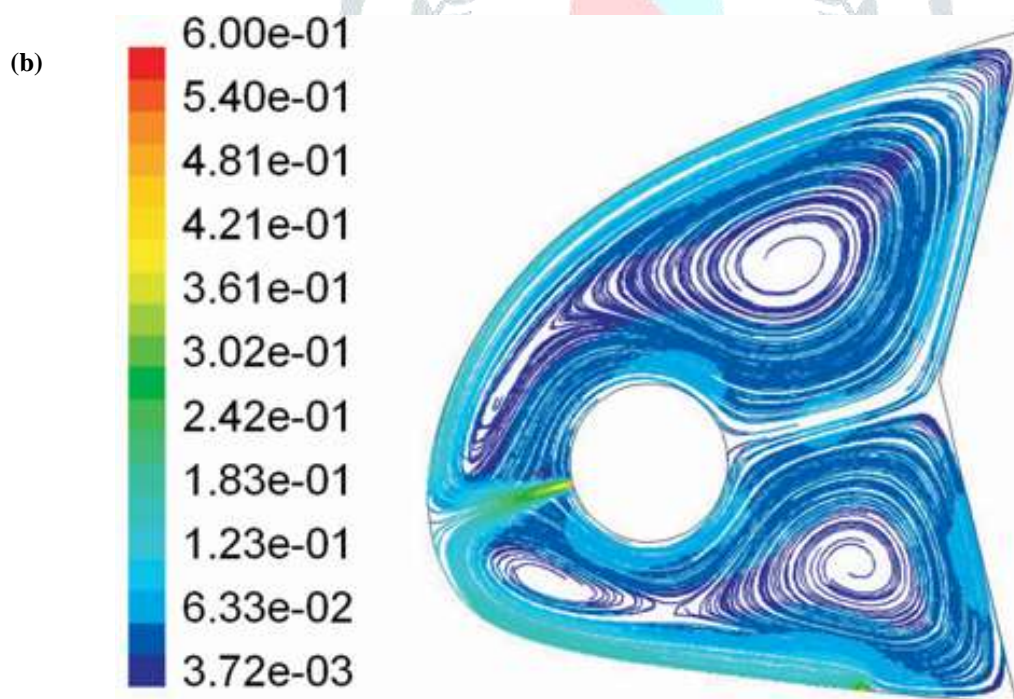


**Figure 5.** Comparison of flow fields colored by Mach number: (a) one Cross section in 3-D bay; (b) corresponding 2-D slice.



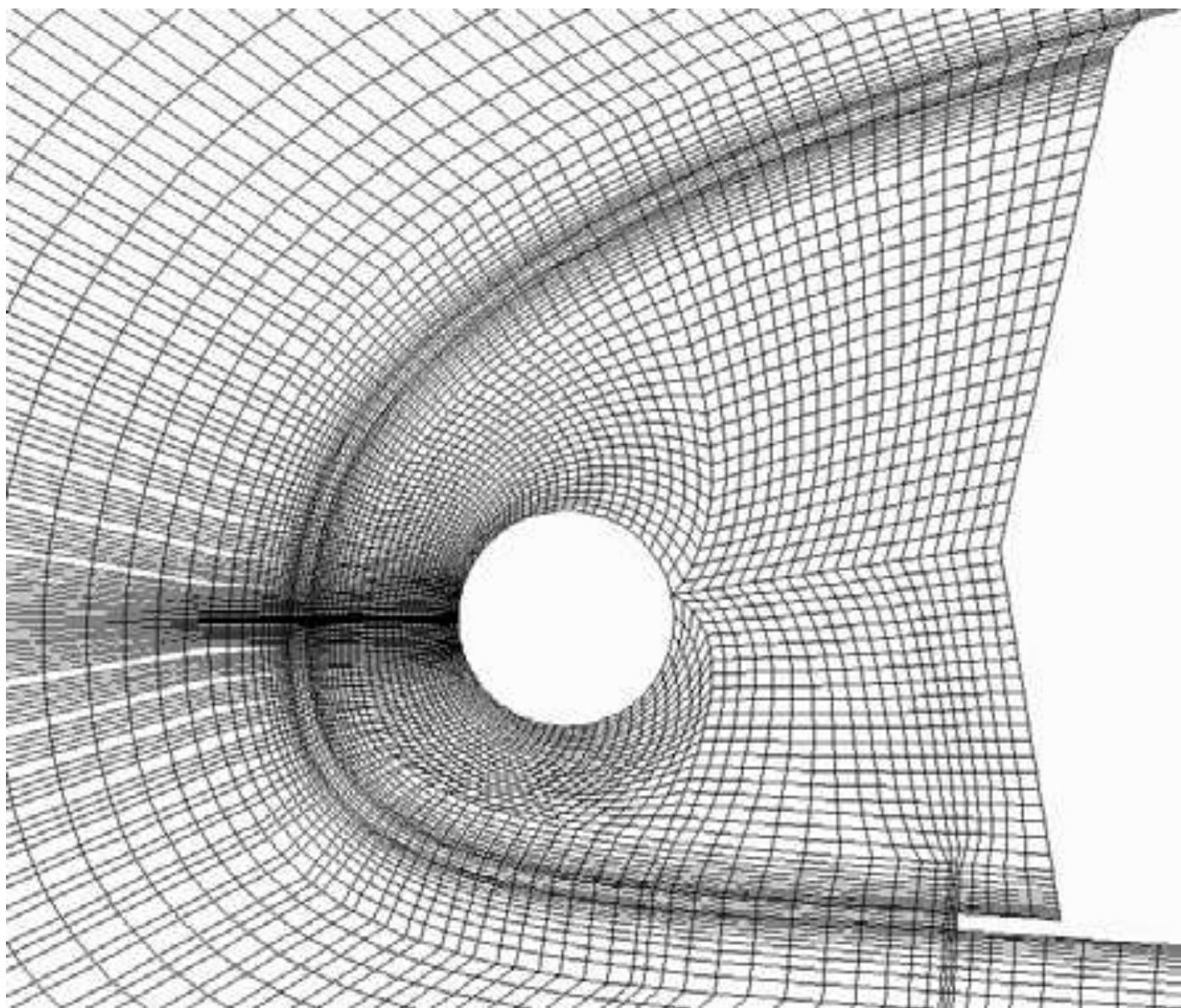


**Figure 6. Part of the structured mesh.**

Seen in both 2-D and 3-D sections. The large vortex in the lower part of the bay behind the piccolo tube exists in both sections. The other large vortex in the upper rear part of the 2-D field does not appear clearly in the 3-D section because of the dominant mixed and cross flow. However, the 3-D skin friction coefficient  $C_f$  appears as low as only approximately  $1/2$  to  $1/3$  the values of the corresponding 2-D computations for the lower surface and only  $1/10$  the values for the upper surface. The only exception is located at the leading edge area where the hot air impinges the internal skin surface, where the 2-D and 3-D values are close. The reason of this 2-D to 3-D discrepancy lies in the difference of the local flow speed, as discussed before. The 2-D flow speed near the inner upper surface is higher than the 3-D values. This phenomenon suggests that the heat transfer might be over-estimated in 2-D results, particularly at the upper surface. Therefore, special attention should be given when one chooses the 2-D approximation model. Data tuning, correction, and validation are necessary when estimating the 3-D bay flows using the 2-D results.

### **III . UNSTEADY THERMODYNAMIC SIMULATIONS & FLOW AND THERMAL ANALYSIS OF THE INTEGRATED INTERIOR-EXTERIOR FLOWS**

#### **3.1. THE NAVIER-STOKES SOLVER**

The CFD method used in this research is a well-known Navier-Stokes solver FLUENT V6.1/6.2<sup>8</sup>. Its reliability has been demonstrated by a great number of aerospace and industrial applications.

#### **3.2. THE BOUNDARY CONDITIONS FOR THE UNSTEADY SIMULATION**

For the integrated internal/external thermal flow simulation, pressure far field boundary condition (B.C.) is used for the external field, which includes the flight Mach number, angle of attack and altitude. Pressure inlet B.C. is given at the Piccolo tube holes, where the total pressure and total temperature change with the regulation of the wing anti-icing valve. Symmetrical B.C.'s

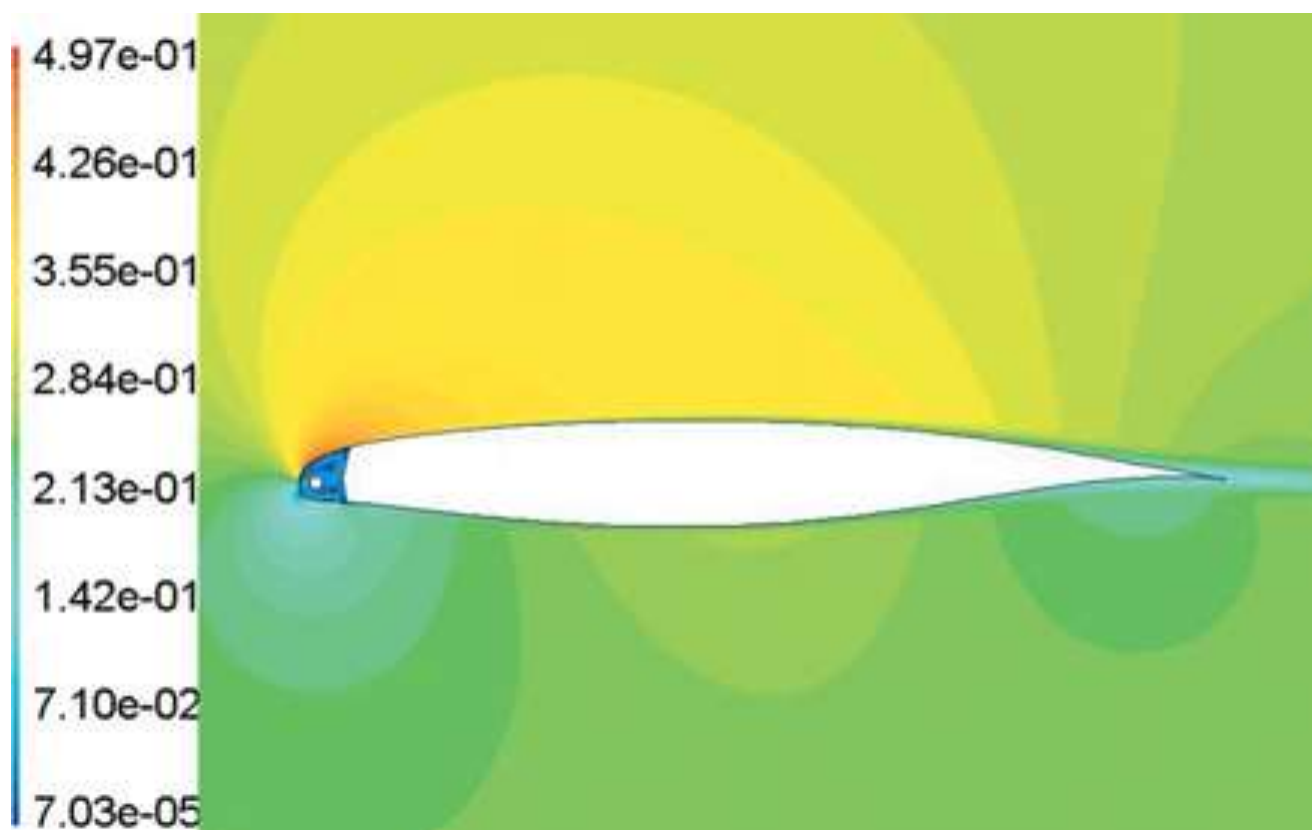


**Figure 7. Mach contours of the interior–exterior flows.**

Are applied on the side faces of the external flow field and the sidewalls of the solid skin. Heat transfer is considered for the inner and outer surfaces of the leading edge skin. Other wing surfaces are treated as adiabatic walls.

On the one hand, most of the anti-icing operations are taking place in the second phase climb and initial phase of cruise, and the far field conditions may not vary sharply. On the other hand, the Piccolo tube pressure and temperature will change quickly with the adjustment of the control valves. In the CFD analysis, the Piccolo tube inlet boundary conditions are controlled by using the user-defined functions (UDF). In this approach, the inlet pressure and temperature are described by functions of time written in C++ language. In each time step of the flow solution, the B.C. values will be calculated and assigned to the solver automatically.

### 3.3. INTEGRATED INTERIOR–EXTERIOR MODEL

To calculate the exterior skin temperature of the wing leading edge, the thermodynamic analysis is applied to a geometry model that is constructed to include both internal and external flows. For the purpose of accurate external flow simulations, the complete wing, or at least a complete wing section, must be taken into account. In this paper, we present an example of such a simulation in two dimensions. A supercritical wing section NPU-SP8 (Hua and Zhang, 1990) is selected and modified so that the leading edge is more close to the above bay model. The aforementioned 2-D bay model is then inserted into the first 7% of the airfoil. It has 1.263 m chord length. The leading edge skin is modeled as a 1.7-mm-thick aluminum sheet. The viscous heat transfer between the skin and the interior–exterior fluid flows and the heat conductivity inside the aluminum skin are included in the simulation. The exterior flow is initiated from a pressure farfield boundary condition. The hot air injection is set up as a pressure inlet condition in the piccolo tube. The interior hot flow and the exterior dry-air flow fields are connected through the exhaust slot in the lower side of the bay. The widths of the injecting and exhaust slots in the 2-D models are chosen to match the total injection and exhaust areas of the 3-D bay. To achieve more accurate simulations of the viscous effect and heat transfer with limited number of grid cells, the structured mesh is generated for both interior and exterior flow fields, as well as inside the solid skin, as partly shown in **Figure 6**. Boundary layer mesh of 20 layers is used over all the wing surfaces, and the grids are refined near the injection and impinging area. There are only 28 575 cells used in the 2-D grid, taking advantage of the structured mesh.

### 3.4. INTERIOR–EXTERIOR THERMAL FLOW ANALYSIS

The far-field flow conditions are defined as follows: Mach number is 0.28, angle of attack is  $4.5^\circ$ , and static pressure is 63 000 Pa and static temperature is 263 K. The hot air inlet condition is chosen the same as in the 3-D bay cases. The pressure outlet condition at the exhaust is not required for this configuration. The CFD simulation presented in this paper is valid only for a dry-air flight. Super-cooled droplet impingement, evaporation, and the icing process are not treated. A typical integrated interior–exterior thermodynamic analysis result is shown in **Figure 7**, plotted as Mach contours. It shows that, compared with the exterior flow, the interior flow is very slow. Three injection slots are located at the front side of the piccolo tube. Two are located at  $15^\circ$  upper and lower positions from the chord direction, respectively, and the third one is set in between, on the chord plane. By specifying either pressure inlet boundary conditions or wall boundary conditions, the injection holes can be activated separately.



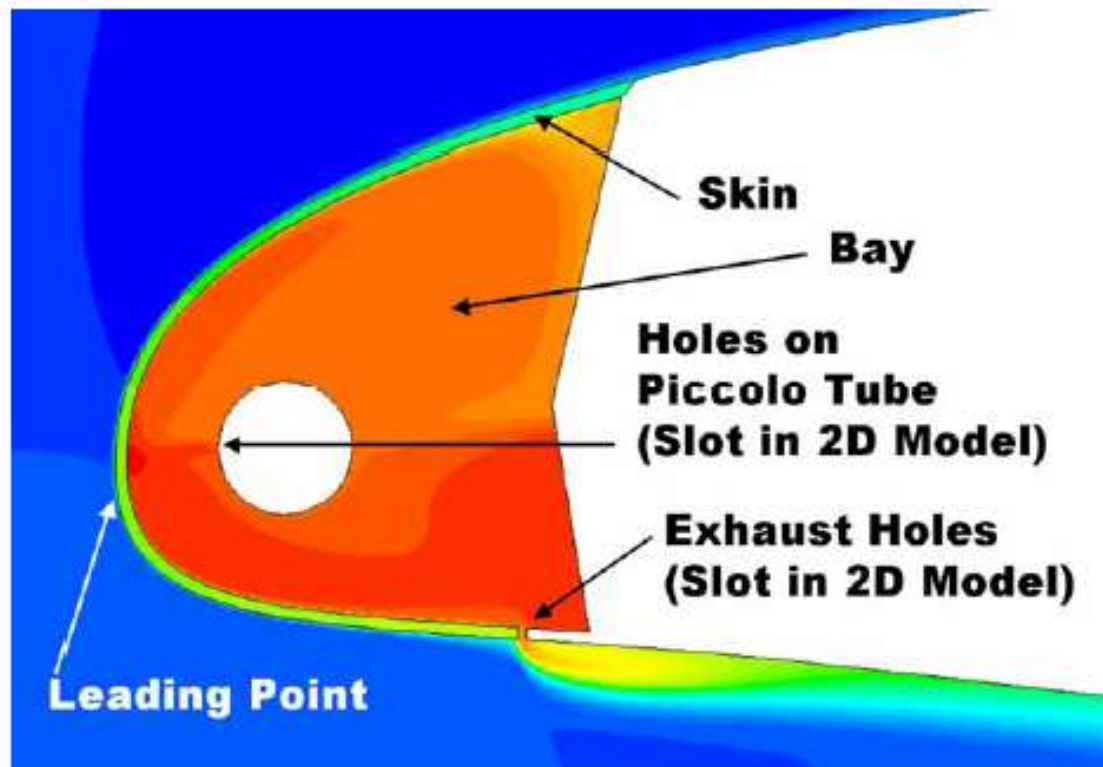


Fig. 7b Temperature contour of the 2D model

### 3.5. UNSTEADY SIMULATION WITH BASIC FUNCTIONS AS THE PICCOLO TUBE INLET CONDITIONS

Most control systems require dynamic input and output variables. In the case of a WAIS, such variables include the pressure and temperature of the piccolo tube, as functions of time. In order to simulate the dynamic functions, one will use the step or exponential functions for approximation. At the initial step of the unsteady investigation, three such functions are selected to describe the Piccolo tube inlet heat fluxes in a 2D model:

- 1) Single Step:  $F(X, t) = X_{t=0} + DX, t > 0$
- 2) Exponent law:  $F(X, t) = X_{t=0} + DX(1 - \exp(-kt)), k = 0.01 \text{ and } 0.5$
- 3) Sin law:  $F(X, t) = X_{t=0} + DX^x \sin(2\pi kt), k = 120$

Where  $X=T_0$  and  $P_0$ ;  $T_{0,t=0} = 453 \text{ K}$ ,  $P_{0,t=0} = 90000 \text{ Pa}$ ;  $DT_0 = 5 \text{ K}$ ,  $DP_0 = 2500 \text{ Pa}$  for all the above cases. Meanwhile, the external flow condition is for flight at  $M=0.31$ ,  $\alpha=4.5^\circ$  and altitude 6500m.

**Fig 7b** is a plot of temperature contour of the 2D model at  $t=200 \text{ sec}$ . In the 2D model, the two staggered rows of small holes on the Piccolo tube are represented with a single slot at zero degree; its width is determined by the sum of the total area of the small holes on the Piccolo tube of one bay. The same assumption is used for the exhaust holes of the bay.

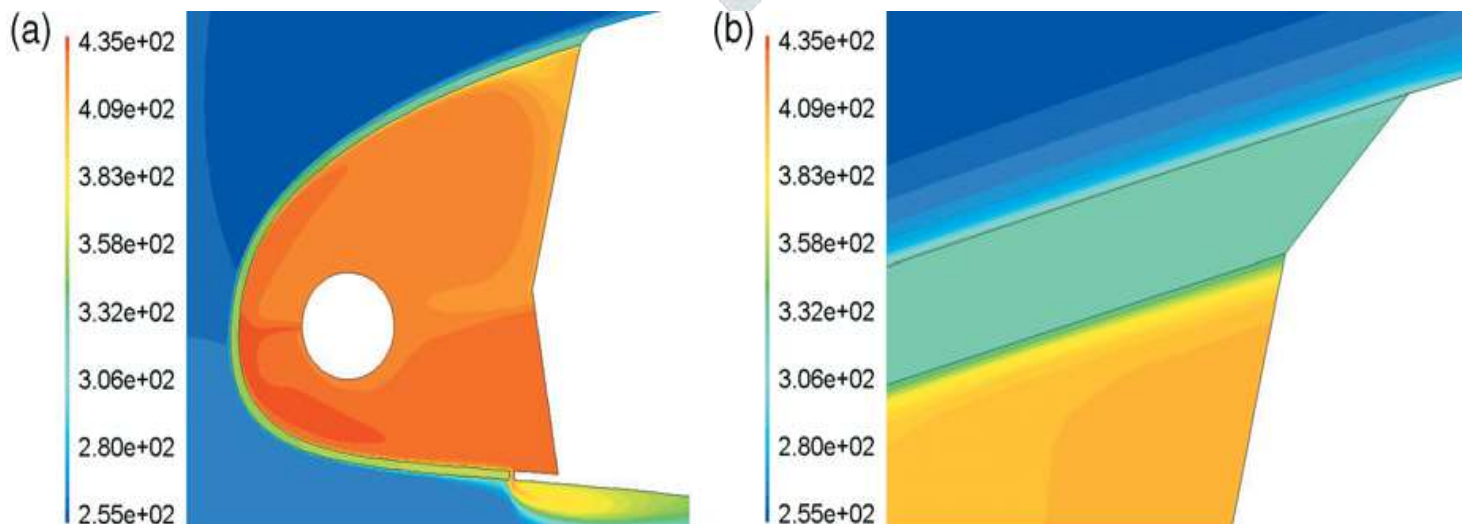


Figure 8. (a) Temperature distributions (K); (b) temperature boundary layers near the upper-rear corner of the bay (K).

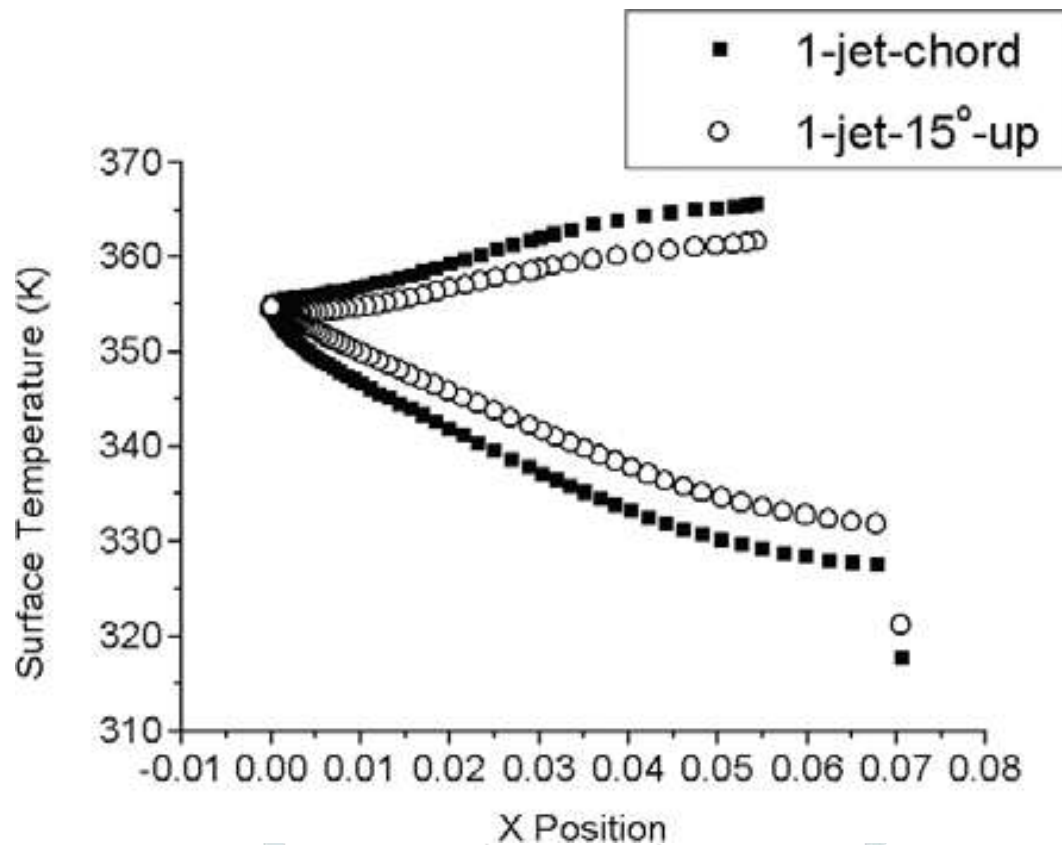


Figure 9. Temperature distributions over the outside surface of the bay For different slots orientations.

This plot shows clearly the hot temperature in the bay, clod external field, skin temperature variation and the merge of the hot exhaust with the external flow. **Figure 8a** shows the static temperature contour of a single injection slot case denoted by “1-jet-chord”. The injection is on the chord direction. The temperature distributions inside the aluminum skin and in both the internal and external flow fields are well illustrated. The temperature boundary layers can be clearly observed in an enlarged part, as shown in **Figure 8b**. The skin temperature decreases towards the upper-rear corner of the bay, as discussed in Sect. 2. The higher local speed

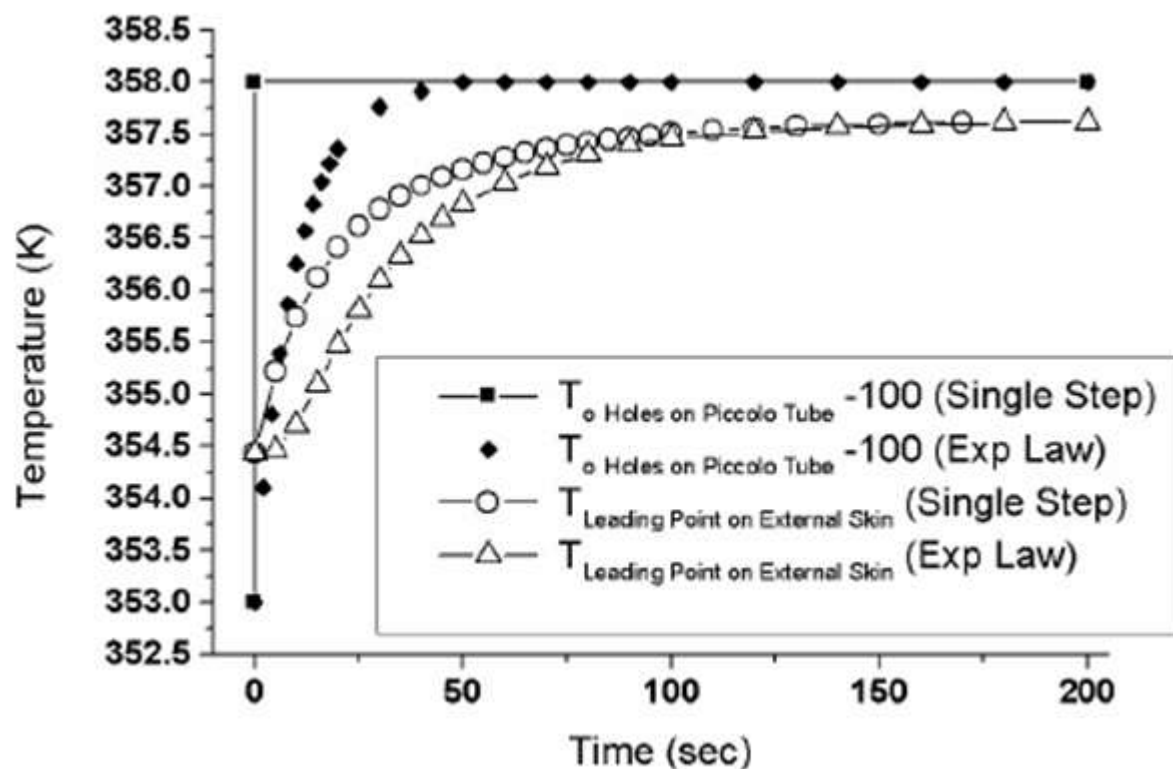
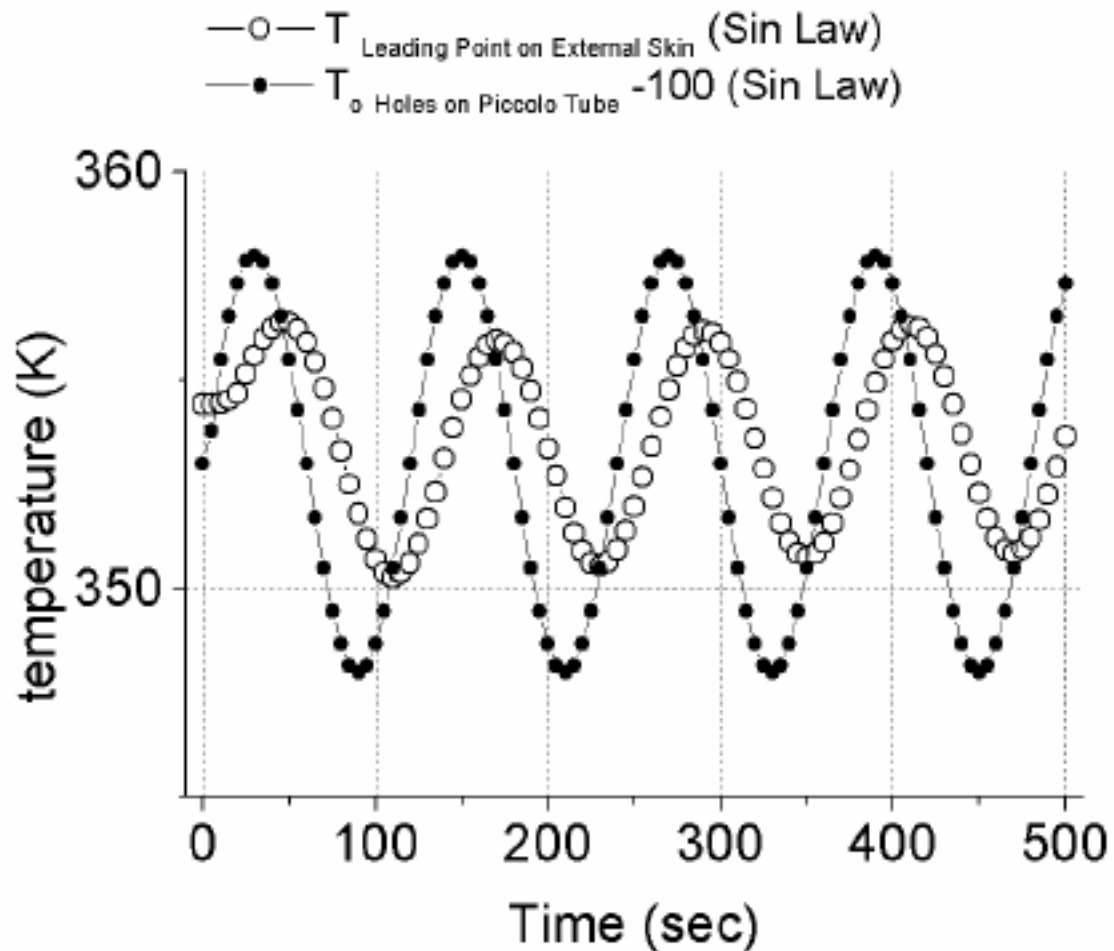


Fig. 9b Skin temperature response to the first two basic functions



Fig. 9c Response of skin temperature at leading point with Sin Law



Of the external flow brings away a lot of heat, and the slow interior flow cannot supply enough heat. As an attempt to increase the temperature near the upper-rear corner, another injection simulation is carried out with the slot located  $15^\circ$  up position to the chord direction, denoted by “1-jet- $15^\circ$ -up”. The temperature over the entire upper skin increases correspondingly, and the temperature of lower surface decreases, as shown in **Figure 9**. Fig 9b shows how the temperature of the skin leading point changes with the

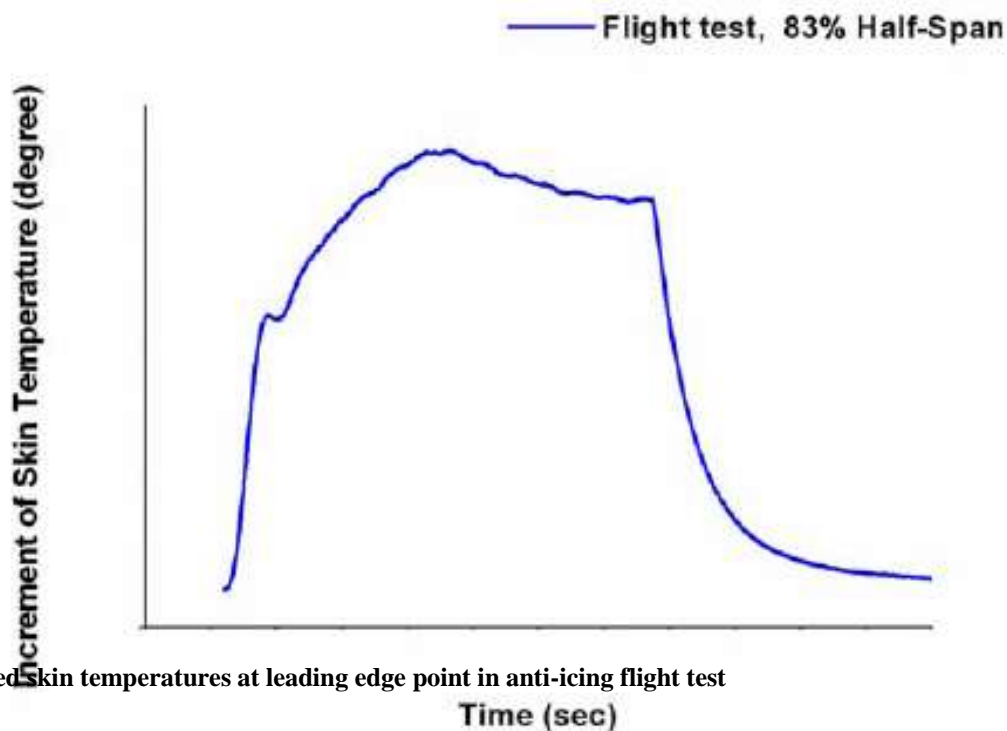


Fig. 10a Measured skin temperatures at leading edge point in anti-icing flight test

Piccolo tube inlet conditions for the first two functions. Fig. 9c shows the external skin temperature at the leading point varying with the Sin Law in the first 500 seconds.

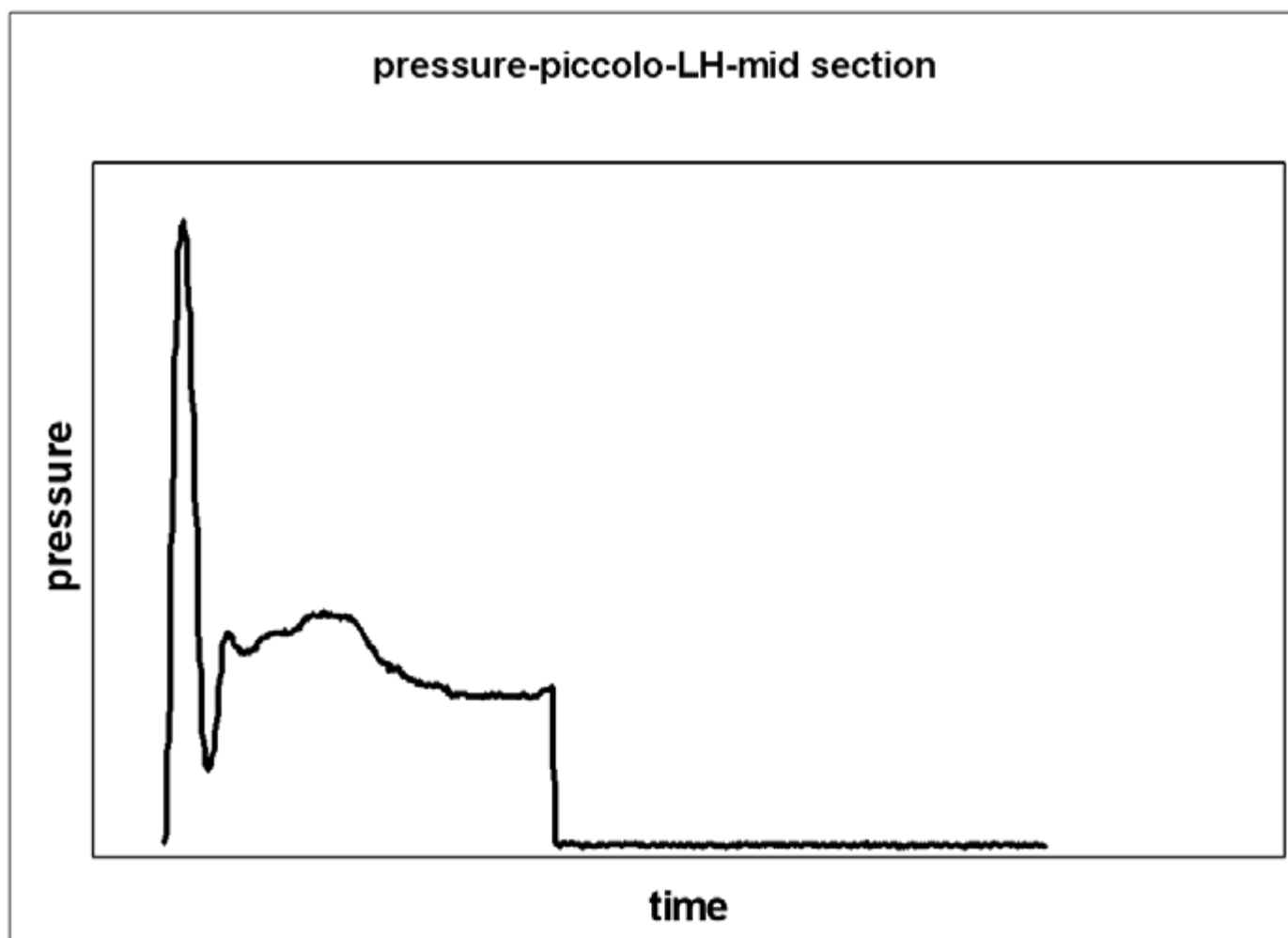


Fig. 10b Measured Piccolo tube pressure in anti-icing flight test

**SOME INTERESTING OBSERVATIONS COULD BE COLLECTED:**

- ✚ The temperature histories of the first two functions converge to the same level and at about same time (the curve plotted here for exponent law is  $k=0.1$ );
- ✚ The maximum increase of the skin temperature is about 3 K, lower than the inlet temperature increment of 5 K, indicating the heat loss carried away by the external flows;
- ✚ The external skin temperature varies also in Sin law shape in the third case;
- ✚ The maximum skin temperature with Sin law is lower than the other two laws as the inlet temperature is changing between +5 and -5 K;
- ✚ The maximum and minimum skin temperature with Sin law is increasing slowly as time goes on;
- ✚ The maximum (peak) values of the injection speed at the small Piccolo tube holes are about 5 seconds delay than the inlet B.C. values, while the peak skin temperature with Sin law is about 20 seconds delay.

**IV. UNSTEADY THERMODYNAMIC SIMULATION OF THE WAIS OPERATION**

Based on the above studies of several basic functions, a 3D WAIS thermodynamic CFD model is used to simulate a complete test loop of the anti-icing operation of a BA business jet in dry air flight tests<sup>9</sup>.

In this test segment, the aircraft is in a steady level flight condition. The WAIV opens and regulates the temperature of the heated leading edge in the anti-icing operation for about 350 seconds, and then shuts down. The wing skin would then cool down as the external flow brings away the remaining heat. **Fig 10a** shows the measured skin temperature of the process at 83% wing span section. Our task is to simulate this test segment with the CFD model.

**4.1. PICCOLO TUBE INLET BOUNDARY CONDITIONS FOR THE SIMULATION**

In the flight tests, pressure and temperature are also measured inside the Piccolo tube, as shown in **Fig 10b** for the pressure at a wing section. These test data are used as the Piccolo tube inlet conditions in the CFD simulation.



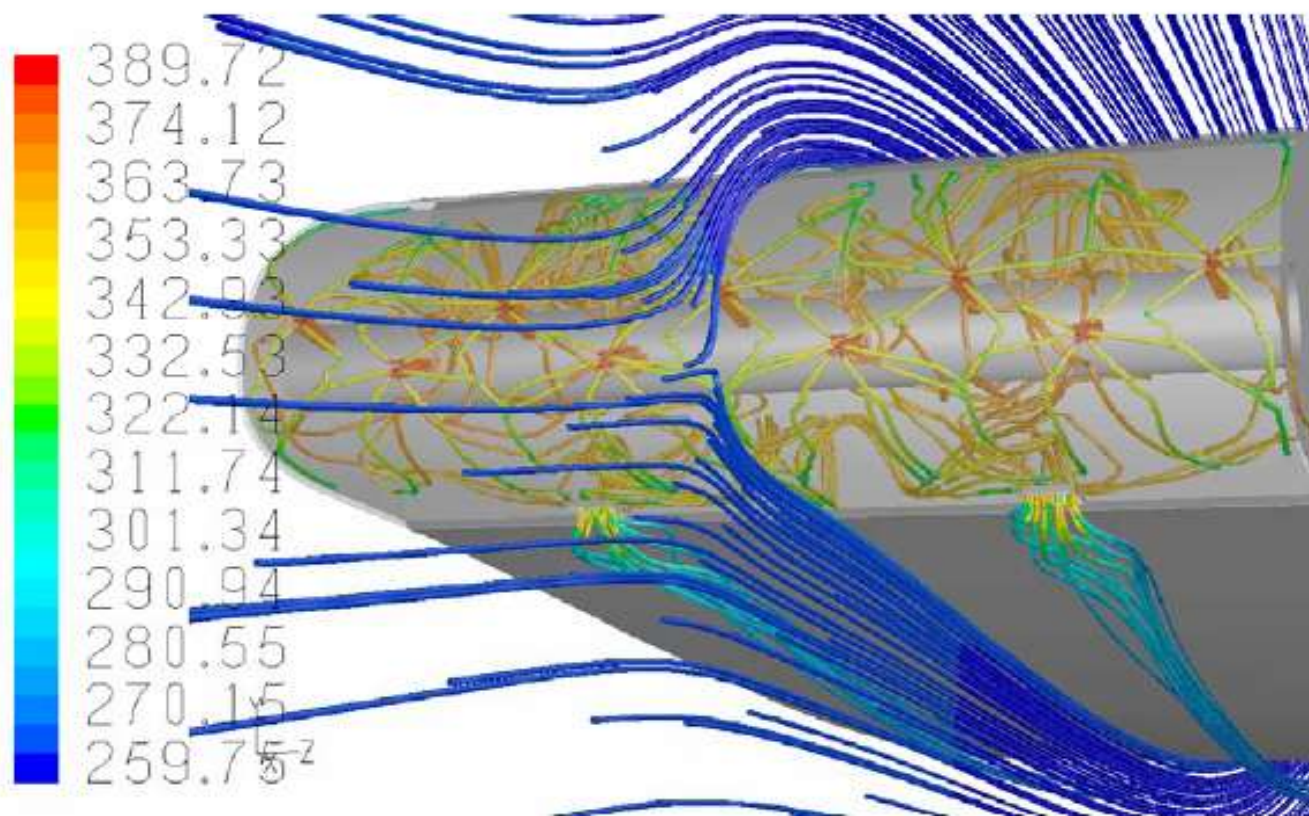


Fig. 11 Streamlines of the CFD simulation colored by temperature (t=36 sec)

From the plot, it could be seen that there is a sharp pulse in the pressure history when the WAIV just opens, and the pressure also drops sharply when the valve shut down. On the contrary, the temperature changes more smoothly with time. Due to the in continuity of the curves, the pressure and temperature variations are converted in to four math functions each. The functions to describe the  $P_0$  and  $T_0$  in the Piccolo tube are written as 4 to 6 order polynomials to represent the values for certain time segment. These math functions are written in C++ programs and coupled with the flow solver as user defined functions.

#### 4.2. NUMERICAL SIMULATION RESULTS

In the simulations, the far field boundary conditions for the external flow are set to be the same as in the flight test. The solver is running in the unsteady implicit segregated scheme and the Spalart-Allmaras turbulent model is used. Second order upwind schemes are selected. The time step is selected as 0.5 second and there are 50 iterations in each time step. **Fig 11** shows the streamlines of the internal and external flows colored by static temperature. It shows how the hot air impinges the inner skin, flows inside the bay and then merges into the cold external flows through the exhaust holes. **Fig 12** plots the total temperature contours at 10 seconds, where the hot air impingement could be identified very well.

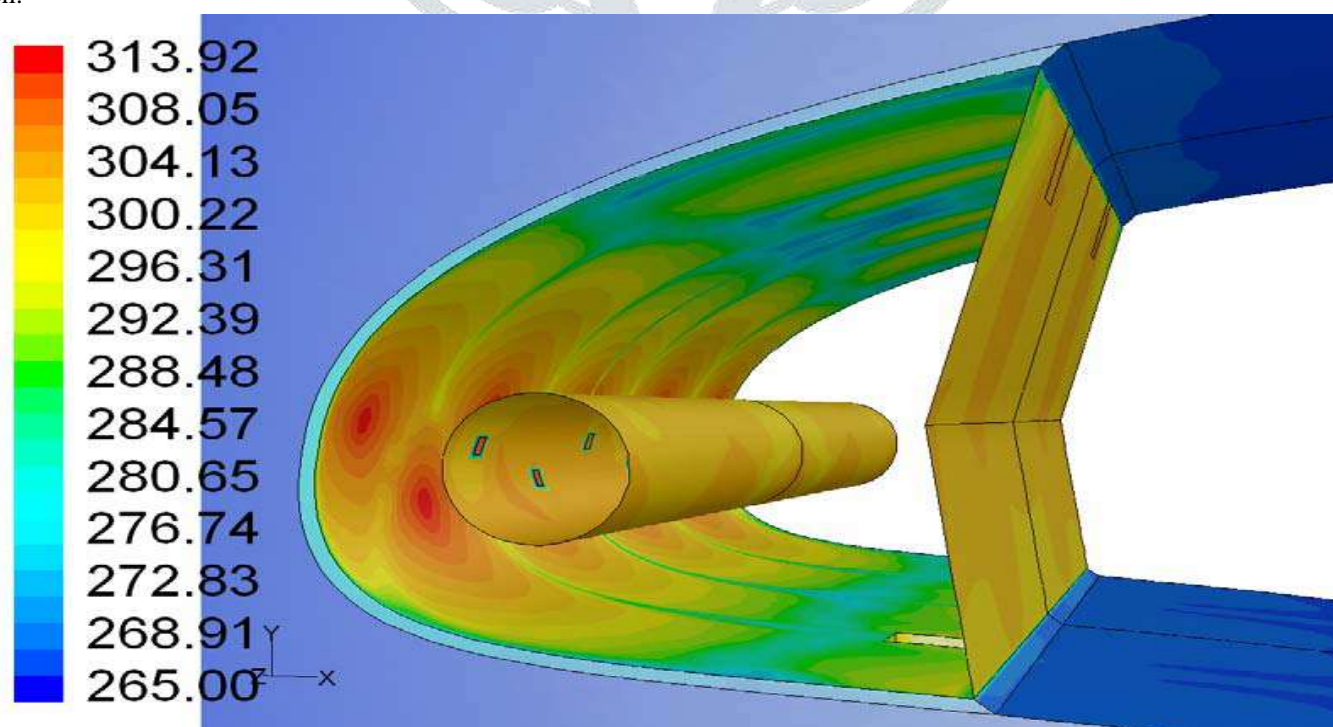
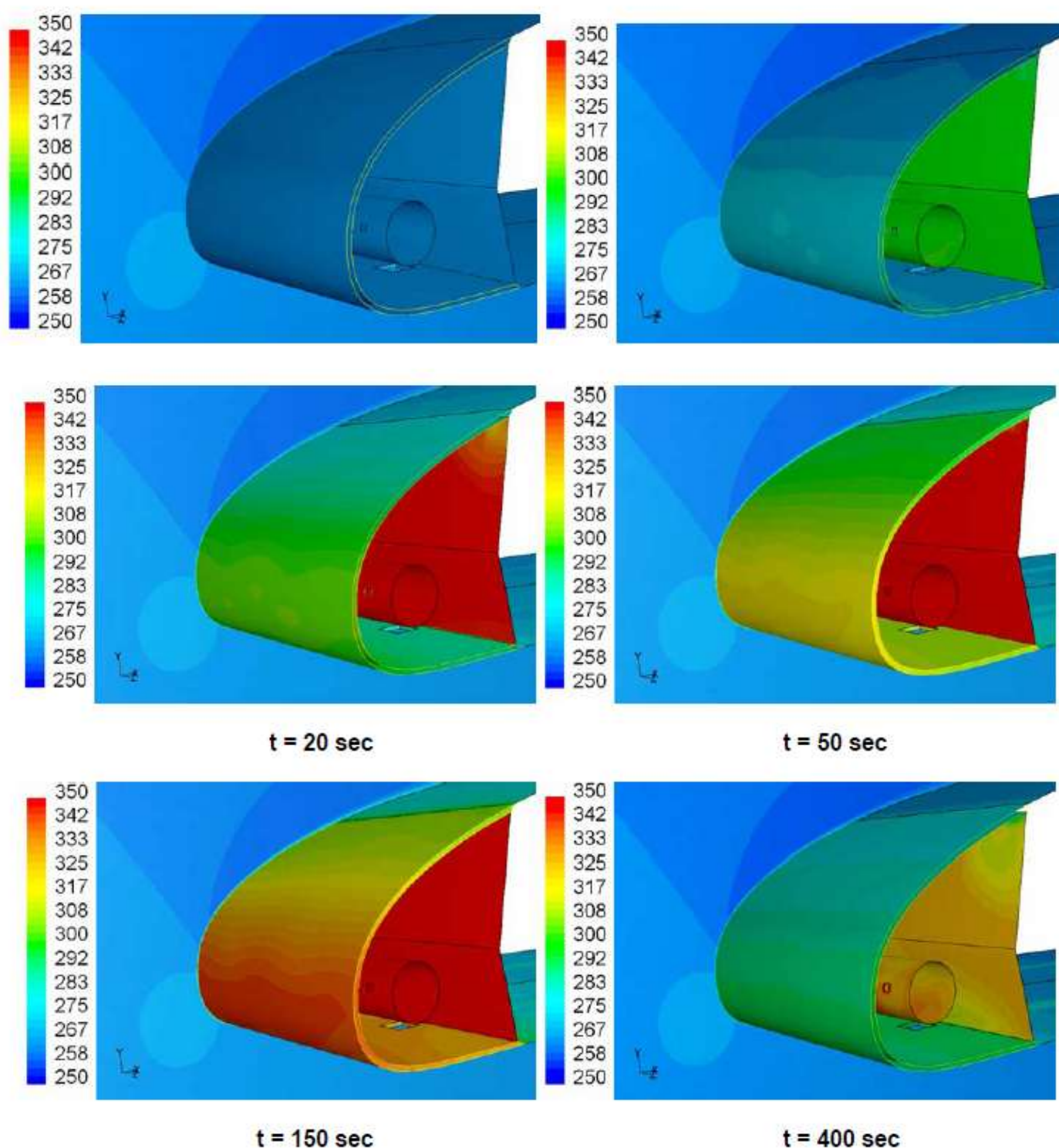


Fig 12 Total temperature contours of the CFD simulation (t=10 sec)

**Fig 13** plots the history of the CFD simulated temperature variation at selected time steps throughout the test loop. The heating and cold down process could be seen clearly by the color, showing the advantage of the CFD at releasing physical details, which may be expensive to obtain by other measurement techniques.



**Fig 13** Skin temperature variation history of the CFD simulation (K) ( $t=0, 10, 20, 50, 150$  and  $400$  seconds)

#### 4.3 COMPARISON WITH FLIGHT TEST

**Fig 14** compares the 2D and 3D CFD unsteady simulations with flight test. The comparison is for the skin temperature at the leading point of the wing where the sensors are located in the flight test. Flight measured history at two span sections are plotted, even though they are very close to each other

It could be seen that the 3D CFD results have excellent coincidence with the flight test, in the entire time segments from the WAIV opening, regulating and shutting down. The 2D CFD results have under estimation at initial time period and over estimation after the flow is set up. The reason for the under estimation at beginning is because there is only one slot on the Piccolo tube in the 2D model and the leading point is lower than the impingement area of the hot jet; while for the over estimation when the flow is well set up, the flow pattern in the 2D bay section is more stable and there is no cross flow, so the energy is better conserved in the 2D model than in the 3D case. Details of discussion can be found in earlier steady flow simulations.



#### 4.4. COMPARISON WITH TEST DATA

The 2-D internal-external coupled CFD results are compared with the available flight test data of an aircraft that has similar anti-icing configuration (Bombardier Aerospace, 2002). The comparison is again for the dry air flight case only. The CFD boundary conditions are set to  $M = 0.31$ , angle of attack  $\alpha = 3.5^\circ$ ,  $P = 63\,000$  Pa, and  $T = 263$  K for external flow;  $T_0 = 454$  K and  $P_0 = 87\,500$  Pa for the internal flow at the piccolo tube holes. Because of the difference in geometry details, and because the exact  $x$  coordinates of the temperature sensors are not specified (it is known only that the sensors in the flight test are located at the leading edge, the upper-rear-end, and the lower rear- end of the bay), the comparison is then limited to the Temperature region only, as shown in **Figure 15**.

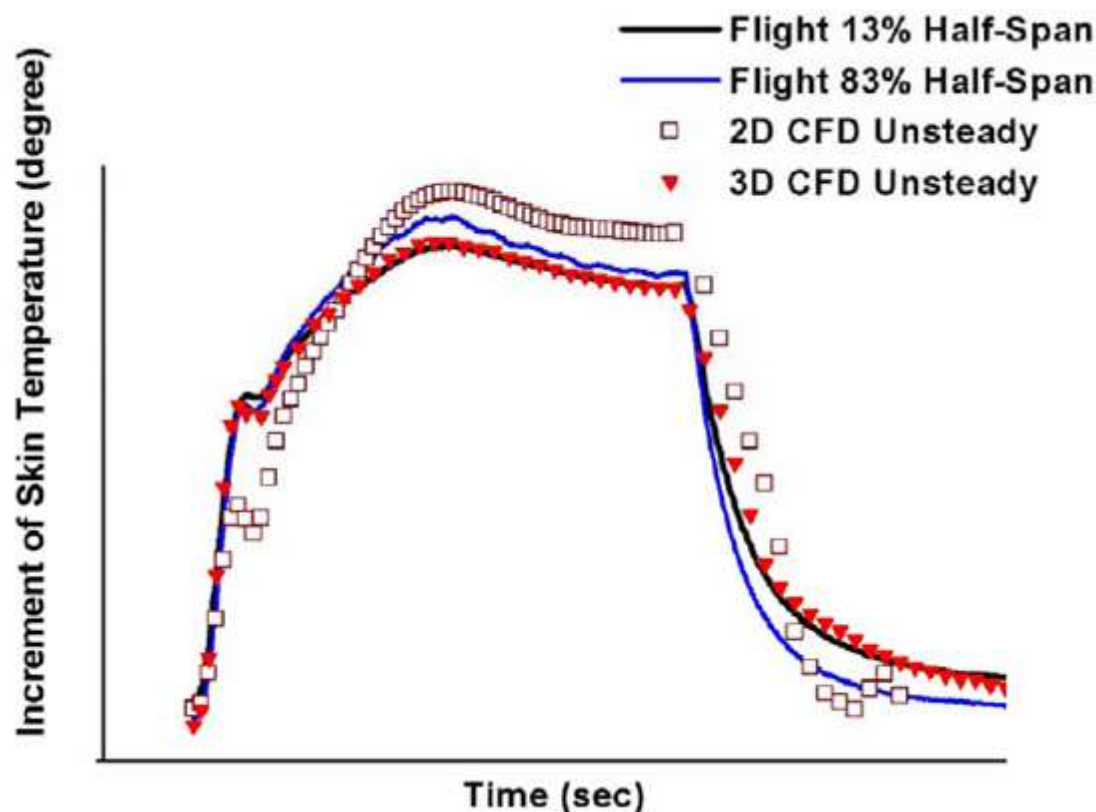


Fig 14 CFD-flight test comparison of skin temperature dynamic variation history

The CFD estimated temperature is very close to the measurement at the leading edge. The upper surface values are overestimated, as we experienced before. The reason for the overestimation of the lower side is the exhaust slot in the 2-D model. The exhaust hot air greatly slows down the lower side flow between the stagnation point and the exhaust slot, leading to less external heat transfer there. The existence of the exhaust slot in the 2-D model also accelerates the internal flow along the lower side, causing more internal heat transfer.

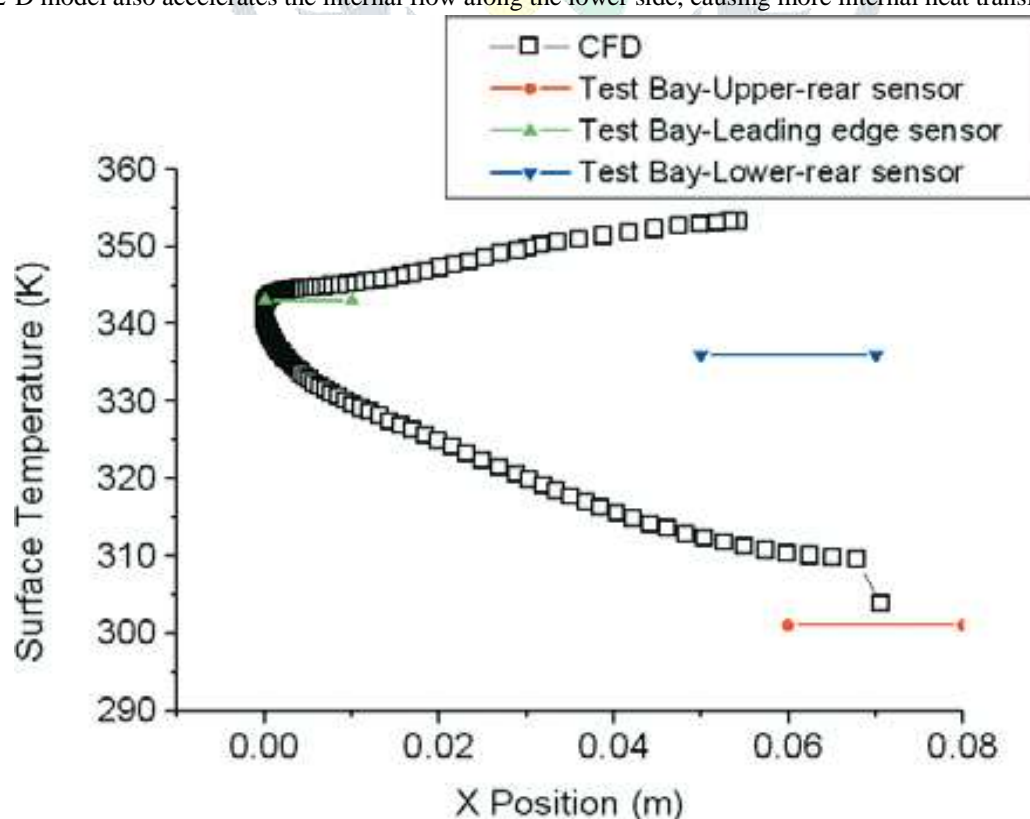


Figure 15. Temperature distributions over the outside surface of the Bay and compared with test data.

## V. CONCLUSIONS

An aircraft wing anti-icing flight test loop has been represented with a 3D unsteady thermodynamic CFD simulation, based on a Navier-Stokes method, following a 2D unsteady investigation of the same problem. The heating process is simulated at the beginning of this study by applying different basic functions presenting Piccolo tube heat flux, and the wing skin responses are discussed. The 3D CFD model involves a complete wing segment with the piccolo type thermal anti-icing bay. In the unsteady integrated internal/external thermal flow simulation with heat conductivity through the solid skin, time dependent boundary condition specifications and proper time steps are investigated. The structured mesh generated increases the unsteady simulations efficiency.

The calculated 3D skin temperature dynamic variation coincides with the flight measurements very well. It indicates the possibility of applying CFD simulation data to the anti-icing system development. It may be used in dynamic model tuning, to complement or even be used in place of the flight test data that are expensive and often not complete enough to serve this purpose. The process of integrating such unsteady CFD simulations into WAIS dynamic model development is currently under investigation.

The 3-D bay flow could be approximately simulated by the corresponding 2-D slice model from the perspective of the flow pattern. Most of the estimated 2-D flow characteristics are within 15% accuracy compared with their 3-D results, except for the surface friction coefficient. The comparisons suggest that the 2-D results may overestimate the internal heat exchange. The data correction and tuning are necessary in practice. The integrated interior–exterior flow analysis of a complete wing section with the inserted leading edge anti-icing bay is conducted. It takes the real skin heat transfer and conductivity into account, so as to obtain the temperature distributions over the skin surface of the bay under actual dry air flight conditions. The surface temperature distributions could be modified for given inlet and far field conditions by adjusting the hot air injection directions. The surface temperature estimated from the 2-D CFD simulation is observed to be within the test data region. However, the upper and lower surface temperature values tend to be overestimated. Future work will include the 3-D

Integrated interior–exterior thermodynamic analysis of a reasonable wing–bay anti-icing system model and unsteady CFD investigations.

## REFERENCES

- [1]. Bombardier Aerospace. (2002). “Wing anti-icing flight test data”. Bourgault, Y., Boutanios, Z., and Habashi, W.G. (2000). 2. [2]. “Threedimensional Eulerian Approach to Droplet Impingement Simulation Using FENSAP-ICE, Part1: Model, Algorithm, and Validation”. *J. Aircr.* Vol. 37, No. 1, pp. 95–103.
- [3]. Beaugendre, H., Morency, F., and Habashi, W.G. (2003). “FENSAP-ICE’s Three-Dimensional in Flight Ice Accretion Module: ICE3D”. *J. Aircr.* Vol. 40, No. 2, pp. 239–247.
- [4]. de Mattos, B.S., and Oliveira, G.L. (2000). “Three-dimensional Thermal Coupled Analysis of a Wing Slice Slat with a Piccolo Tube”. *Proceedings of the AIAA Applied Aerodynamics 18th Conference*, Denver, Colorado, 14-17 August 2000. AIAA-2000-3921.
- [5]. Bourgault, Y., Boutanios, Z. and Habashi, W.G., “Three-dimensional Eulerian Approach to Droplet Impingement Simulation Using FENSAP-ICE, Part1: Model, Algorithm, and Validation”, *Journal of Aircraft*, Vol. 37, No. 1, pp 95-103, 2000.
- [6]. Beaugendre, H., Morency, F. and Habashi, W.G., “FENSAP-ICE’s Three-Dimensional In-Flight Ice Accretion Module: ICE3D”, *Journal of Aircraft*, Vol.40, No.2, pp 239-247, 2003.
- [7]. Bidwell, C.S., Pinella, D. and Garrison, P., “Ice Accretion Calculations for a Commercial Transport Using the LEWICE3D, ICEGRID3D and CMARC Programs”, NASA/TM-1999-208895, 1999.
- [8]. Morency, F., Tezok, F. and Paraschivoiu, I., “Heat and Mass Transfer in the Case of Anti-Icing System Simulation”, *Journal of Aircraft*, Vol. 37, No.2, pp245-252, 2000.
- [9]. Fluent V6.0. Available from <http://www.fluent.com> [accessed 2002]. Frick, C.W., Jr., and McCullough, G.B. (1942). “A Method for Determining the Rate of Heat Transfer from a Wing or Streamline Body”. NACA Report 830. Hua, J., and Zhang, Z.Y. (1990). “Transonic Wing Design for Transport Aircraft”. ICAS-90–3.7.4.
- [10]. Liu, H.H.T. and Hua, J., “Three-Dimensional Integrated Thermodynamic Simulation for Wing Anti-Icing System”, *Journal of Aircraft*, Vol. 41, No. 6, pp 1291-1297, 2004.
- [11]. Hua, J. and Liu, H.H.T., “Fluid Flow and Thermodynamic Analysis of a Wing Anti-Icing System”, *Canadian Aeronautics and Space Journal*, Vol. 51, No. 1, pp 35-40, 2005.
- [12]. Fluent V6 User Guide, 2003.
- [13]. Bombardier Aerospace, “Flight Test Data of Wing Anti-Icing System”, Internal Communication, 2003.
- [14]. Simulation Using CANICE”. *J. Aircr.* Vol. 36, No. 6, pp. 999–1006,
- [15]. Wang, D., Naterer, G.F., and Wang, G. (2003). “Thermo fluid Optimization of a Heated Helicopter Engine Cooling-Bay Surface”. *Can. Aeronaut. Space J.* Vol. 49, No. 2, pp. 73–86.